


## Element-selective investigation of femtosecond spin dynamics in NiPd magnetic alloys using extreme ultraviolet radiation

Seung-gi Gang,<sup>\*</sup> Roman Adam,<sup>†</sup> Moritz Plötzing, Moritz von Witzleben, Christian Weier, Umut Parlak, Daniel E. Bürgler, and Claus M. Schneider

*Peter Grünberg Institut PGI-6, Research Centre Jülich, 52425 Jülich, Germany*

Jan Rusz, Pablo Maldonado, and Peter M. Oppeneer

*Department of Physics and Astronomy, Uppsala University, P.O. Box 516, 75120 Uppsala, Sweden*

 (Received 3 November 2017; revised manuscript received 25 January 2018; published 20 February 2018)

We studied femtosecond spin dynamics in  $\text{Ni}_x\text{Pd}_{1-x}$  magnetic thin films by optically pumping the system with infrared (1.55 eV) laser pulses and subsequently recording the reflectivity of extreme ultraviolet (XUV) pulses synchronized with the pump pulse train. XUV light in the energy range from 20 to 72 eV was produced by laser high-harmonic generation. The reflectivity of XUV radiation at characteristic resonant energies allowed separate detection of the spin dynamics in the elemental subsystems at the  $M_{2,3}$  absorption edges of Ni (68.0 and 66.2 eV) and  $N_{2,3}$  edges of Pd (55.7 and 50.9 eV). The measurements were performed in transversal magneto-optical Kerr effect geometry. In static measurements, we observed a magnetic signature of the Pd subsystem due to an induced magnetization. Calculated magneto-optical asymmetries based on density functional theory show close agreement with the measured results. Femtosecond spin dynamics measured at the Ni absorption edges indicates that increasing the Pd concentration, which causes a decrease in the Curie temperature  $T_C$ , results in a drop of the demagnetization time  $\tau_M$ , contrary to the  $\tau_M \sim 1/T_C$  scaling expected for single-species materials. This observation is ascribed to the increase of the Pd-mediated spin-orbit coupling in the alloy.

DOI: [10.1103/PhysRevB.97.064412](https://doi.org/10.1103/PhysRevB.97.064412)

### I. INTRODUCTION

In recent years, studies of optically induced spin dynamics in magnetic materials generated a number of extraordinary results, continuously extending the amount of knowledge and contributing to the improved understanding of the underlying physical mechanisms. At the same time, optical control of the electron spin promises novel applications in energy-efficient data storage and processing. The most widespread technique for femtosecond-time-scale spin dynamics studies employs the time-resolved magneto-optical Kerr effect (MOKE) using pulsed lasers in the visible spectral range ( $\lambda \sim 400\text{--}700$  nm) [1–4]. This approach, however, delivers an integral response of the entire system studied and therefore is blind to possible differences in the response of elemental or structural subsystems of an explored material. In order to gain a deeper insight into the underlying physics, spin dynamics can be probed using laser-generated extreme ultraviolet (XUV) photons. The radiation at these energies can be tuned to the characteristic response of elemental subsystems by probing shallow core levels of individual magnetic elements in alloys [5,6] and multilayered structures [7–11].

A relatively large number of theoretical studies and experiments suggested that, apparently, more than one physical mechanism is responsible for the spin dynamics in magnetic materials. Currently, Elliott-Yafet-type electron-phonon

scattering [12] and superdiffusive spin transport [7,8,13,14] are among the most actively pursued descriptions of the physical origins of ultrafast demagnetization. In the latter case, neighboring layers and substrate material play a crucial role in the spin dynamics response. The authors of Ref. [12] consider electron-phonon spin-flip scattering combined with a microscopic three-temperature model (M3TM) as a mechanism responsible for spin dissipation on ultrafast time scales. In this model, the demagnetization time  $\tau_M$  scales as  $\tau_M \sim \mu_{AT}/a_{sf}T_C$ , where the atomic magnetic moment  $\mu_{AT}$ , the spin-flip scattering probability  $a_{sf}$ , and the Curie temperature  $T_C$  play a decisive role in setting the time scale of the ultrafast spin dynamics [12]. As a consequence, a higher  $T_C$  is expected to lead to shorter  $\tau_M$  for materials with similar  $a_{sf}$ . In addition, it has been shown recently that the elemental sublattices with different magnetic moments forming an alloy may show distinct element-specific spin dynamics below 1 ps [6,15]. At longer time scales ( $>1$  ps) and close to  $T_C$ , the demagnetization time was shown to depend on the magnetic coupling, resulting in a drop in  $\tau_M$  for antiferromagnetically coupled sublattices [16–18].

The authors of Ref. [19] investigated element selectively the spin dynamics in chemically inhomogeneous GdFeCo ferrimagnets and observed that strong laser pumping results in angular momentum redistribution between Gd and lattice reservoirs and a *lateral flow* of spin angular momentum from Fe-rich into Gd-rich nanoregions. Even though both the Fe-rich and Gd-rich regions were excited by the same laser pulse train, Fe turned out to act as a spin source, and conversely, Gd acted as a spin sink. Superdiffusive spin currents [7,8] can transfer spin angular momentum between spatially separated metallic

<sup>\*</sup>s.gang@fz-juelich.de

<sup>†</sup>r.adam@fz-juelich.de

layers but are generally possible only because spin-majority electrons, even if excited with the same laser power, have a longer mean free path and different velocity than minority-spin electrons [7,13]. It remains an open question whether a similar physical picture can be applied to homogeneous multicomponent alloys. Another possible way of spin angular momentum transfer in multicomponent alloys was proposed by Bar'yakhtar and collaborators, who predicted that exchange-interaction-related spin relaxation could cause longitudinal spin dissipation of atomic moments leading to local spin currents between atoms [17,20].

Here we address this question by studying the ultrafast laser-induced spin dynamics in homogeneous  $\text{Ni}_x\text{Pd}_{1-x}$  alloys and test whether either Ni or Pd could serve as a spin source or spin sink. In addition, the interplay of  $T_C$ ,  $\mu_{\text{AT}}$ , and  $a_{\text{sf}}$  with increasing Pd content is expected to strongly affect the system's response. To gain further insight into the optically triggered spin dynamics, we employed femtosecond pulses of XUV light to element-selectively inspect the spin dynamics of the Ni subsystem for varying Pd content in the alloy. In addition, we performed *ab initio* calculations of the XUV magneto-optical response to trace the origin of features in the static transversal MOKE (T-MOKE) spectra. To investigate the role of spin-orbit coupling in femtosecond demagnetization dynamics the experimental data were compared to M3TM theory [12].

## II. SAMPLES

$\text{Ni}_x\text{Pd}_{1-x}$  alloys form a solid solution over almost the entire range of Pd concentration, and the alloys exhibit ferromagnetic properties up to 98% of Pd in the alloy [21]. For the present studies we fabricated a range of  $\text{Ni}_x\text{Pd}_{1-x}$  thin films by molecular beam epitaxy at a base pressure of  $5 \times 10^{-11}$  mbar. The film thickness of all films and for all stoichiometries was fixed at 20 nm. This thickness corresponds to the second maximum of the oscillatory reflectivity versus thickness curve for XUV light as calculated using the IMD software package [22]. The XUV light from the high-harmonic-generation setup covers the energy range from 20 to 75 eV. For the present experiments we use photons in the energy range from 40 to 75 eV. The attenuation length of XUV light in this energy range in  $\text{Ni}_{0.5}\text{Pd}_{0.5}$  is calculated using dedicated software [23] to lie between 7.8 and 8.5 nm; that is, it is much shorter than the film thickness. Therefore, the influences of the film-substrate interface and the thickness dependence of the transverse Kerr effect are rather small and have not been taken into account in this study to keep the arguments as simple as possible. As Ni and Pd are in the same group of the periodic table, their isoelectronic properties allow for a homogeneous mixing as well as Curie temperature  $T_C$  tuning by varying the Ni-to-Pd mixing ratio in a broad range of temperatures, in our studies from  $T_C \sim 450$  K ( $x \sim 0.5$ ) to  $T_C \sim 630$  K ( $x = 1.0$ , pure nickel) [24]. Furthermore, Pd is easily polarizable and thus readily acquires a magnetic moment when exchange coupled to Ni [25]. The latter accounts for the fact that even though the Pd concentration can increase from 0% to 45%, the magnetic moment in the alloy at the same time decreases only by less than 10% [24].

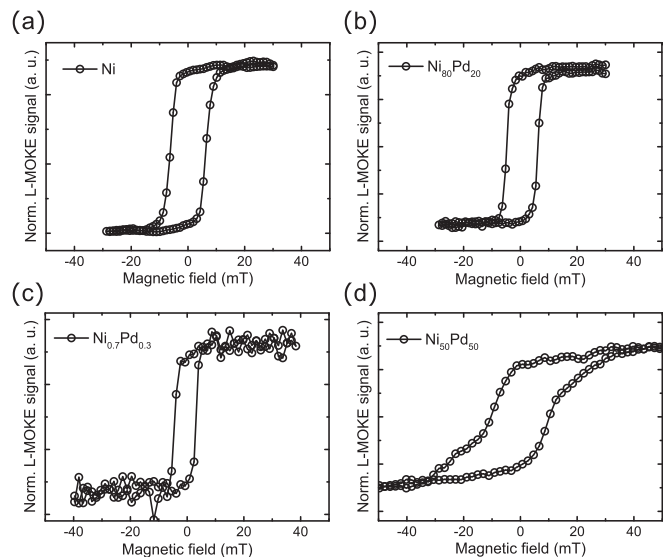


FIG. 1. In-plane magnetization loops of (a) pure Ni and  $\text{Ni}_x\text{Pd}_{1-x}$  alloys with (b)  $x = 0.8$ , (c)  $x = 0.7$ , and (d)  $x = 0.5$  measured using L-MOKE, indicating a predominantly in-plane magnetization orientation for Pd concentrations below 50% ( $x > 0.5$ ).

In our current experiment  $\text{Ni}_x\text{Pd}_{1-x}$  thin-film alloys with Pd concentration ranging from 0% to 50% have been examined using element-selective T-MOKE measurements, probing excitations at the  $N_{2,3}$  edges of Pd and the  $M_{2,3}$  edges of Ni. For Pd concentrations exceeding 50% ( $x < 0.5$ ), the magnetic moment of the alloys turns out of plane, thus making the T-MOKE measurements impossible due to the geometry requirements (see Sec. III).

To characterize the magnetic properties of our films we recorded magnetization curves using the longitudinal MOKE (L-MOKE) employing a 780-nm laser for pure Ni ( $x = 1.0$ ) and three different  $\text{Ni}_x\text{Pd}_{1-x}$  alloy stoichiometries ( $x = 0.8, 0.7, \text{ and } 0.5$ ). The measurements shown in Fig. 1 reveal a clear in-plane orientation of the sample magnetization for  $x = 1.0, 0.8, \text{ and } 0.7$  with a coercive field  $H_C \sim 10$  mT. For  $x = 0.5$  the sample magnetization saturates only at a much higher field of  $H_C \sim 40$  mT, and in addition, the very gradual magnetization increase suggests slow magnetization rotation with increasing field from the slightly out of plane to the in-plane configuration, i.e., along the external field. The measured samples were fabricated on top of *prepatterned* Si/SiO<sub>2</sub> substrates, forming an optical grating with a period of  $2 \mu\text{m}$  for XUV light dispersion. The transient T-MOKE response of a Ni film on a flat, nonpatterned Si/SiO<sub>2</sub> substrate after optical pumping with a given pumping fluence is the same as for a Ni film on a prepatterned substrate excited with the same pumping fluence. This ensures that the grating structure has no measurable influence, either on the pumping beam intensity profile or on the spin dynamics.

## III. EXPERIMENTAL SETUP

In our experiment (see Fig. 2), XUV light is generated by focusing laser light from a laser amplifier (35-fs pulse width, 2 mJ per pulse, 3-kHz repetition rate, 780-nm central wavelength) into a glass capillary filled with a noble gas

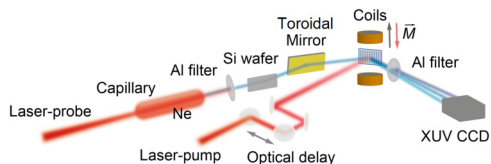


FIG. 2. Experimental setup. The laser pump and XUV probe beams are derived from a single laser amplifier to minimize time jitter. The XUV light propagates in vacuum ( $\sim 10^{-5}$  mbar) and contains a spectrum of photons with energies between 20 and 72 eV. The magnetic field aligns the sample magnetization  $M$  along the direction transversal to the reflection plane.

(Ne) [26]. After the capillary the XUV spectrum (20–72 eV) is separated from the driving laser light by a 150-nm thin Al filter and a Si/SiO<sub>2</sub> rejection wafer. Then either the XUV beam is monochromatized by a pair of Bragg mirrors (not shown in Fig. 2), or alternatively, the entire spectrum is directed onto the sample. The first approach was used for films on flat substrates to address a Ni elemental subsystem. The second approach was used for films on prepatterned substrates, which form an optical grating allowing for energy separation due to dispersion. The incident angle of the XUV beam with respect to the sample normal was fixed near 45° in order to optimize the magnetic signal of Ni [6,7,27–29]. The reflected light was in both configurations recorded by a XUV-sensitive, low-noise charge-coupled device (CCD) camera cooled to 243 K. During all measurements, the magnetic samples were saturated by a magnetic field of  $\mu_0 H = 77$  mT parallel to the sample surface and perpendicular to the XUV reflection plane. All measurements were performed at room temperature. In order to detect the T-MOKE signal, spectral changes at the absorption edges of Ni and Pd were recorded at two magnetic fields with opposite orientations. The magnetic asymmetry  $A$  due to the T-MOKE can be expressed as

$$A = \frac{I(H^\uparrow) - I(H^\downarrow)}{I(H^\uparrow) + I(H^\downarrow)}, \quad (1)$$

where  $A$  is the magnetic asymmetry and  $I(H^\uparrow)$  and  $I(H^\downarrow)$  are the reflected intensities measured at magnetic fields with opposite orientations [28].

An example of the spectra recorded after XUV reflection from a Ni<sub>0.8</sub>Pd<sub>0.2</sub> film deposited on top of the substrate with prepatterned grating is shown in Fig. 3(a). We note that because of the relatively steep slopes of the spectral peaks, a small energy shift between the spectra recorded at  $H^\uparrow$  and  $H^\downarrow$  may cause sharp spikes in the magnetic asymmetry calculation that are not related to magnetic asymmetry. This energy shift (usually smaller than one pixel of the CCD chip) can be corrected by a small (subpixel) shift of the spectra.

## IV. EXPERIMENTAL RESULTS

### A. Static magnetic asymmetry

It was observed earlier that the  $M_{2,3}$  absorption edges of magnetic transition metals are relatively broad, usually extending a few eV around the corresponding tabulated absorption energies [7,27–29]. Element selectivity in our experiment is based on the observation of a strongly increased

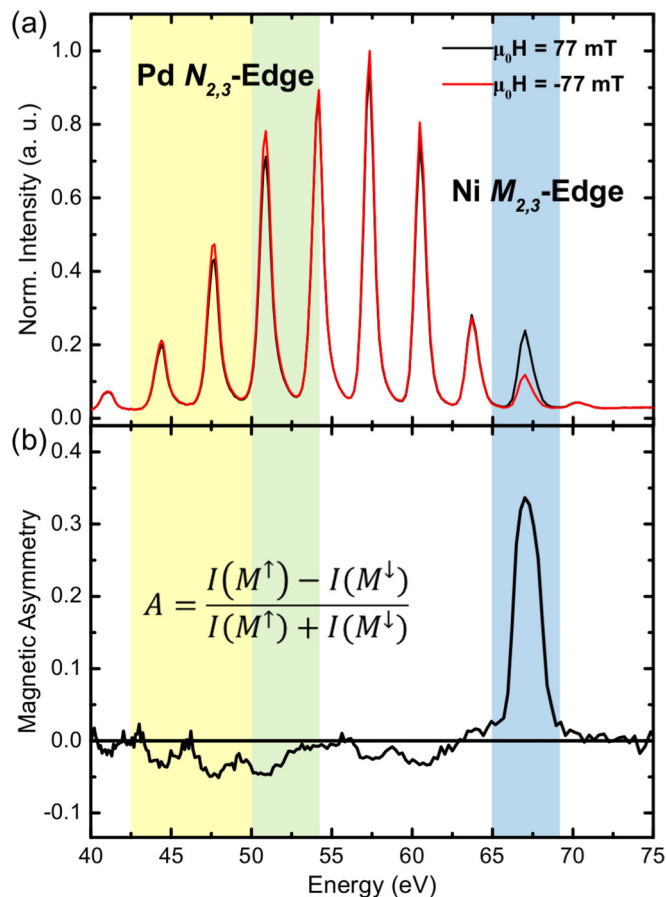


FIG. 3. (a) XUV reflectivity spectra of the Ni<sub>0.8</sub>Pd<sub>0.2</sub> alloy, recorded in the static T-MOKE configuration at a magnetic field oriented “up” (black) and “down” (red) with respect to the plane of incidence and covering both the Ni  $M_{2,3}$  edge (67 eV, blue area) and the Pd  $N_{2,3}$  edge ( $\sim 51$  eV, green area). The yellow area marks the energy interval below the tabulated Pd  $N_{2,3}$  edge. (b) Dimensionless magnetic asymmetry  $A$  of Ni<sub>0.8</sub>Pd<sub>0.2</sub> calculated from the spectra in (a) according to Eq. (1).

magnetic asymmetry measured by the XUV light *tuned to the absorption edge* of a particular element. To have clear access to an elemental subsystem in a multielement compound, the resonant energies of the involved elements should not energetically overlap. In Ni<sub>x</sub>Pd<sub>1-x</sub> alloys, static magnetic asymmetries at the nickel  $M_{2,3}$  and palladium  $N_{2,3}$  edges were obtained from recorded spectra using Eq. (1). Figure 3(a) shows the XUV spectra after reflection from a Ni<sub>0.8</sub>Pd<sub>0.2</sub> film deposited on top of the substrate with prepatterned grating. The measurement for this particular sample stoichiometry yields magnetic asymmetries of up to  $A \sim 33.7\%$  and  $4.6\%$  at the Ni  $M_{2,3}$  edge and Pd  $N_{2,3}$  edge, respectively [Fig. 3(b)]. The magnetic asymmetry between 56 and 61 eV shows a weak negative value, which we relate to the negative part of the bipolar signal at the Ni absorption edge [27]. For the dynamics measurements (see Secs. IV B and IV C) only the positive part of the asymmetry, i.e., the energy interval  $67 \pm 2$  eV (blue area in Fig. 3), is taken into account. Upon increasing the Pd content, the magnetic asymmetry near the Pd  $N_{2,3}$  absorption edge becomes more pronounced (Fig. 4) and in all recorded

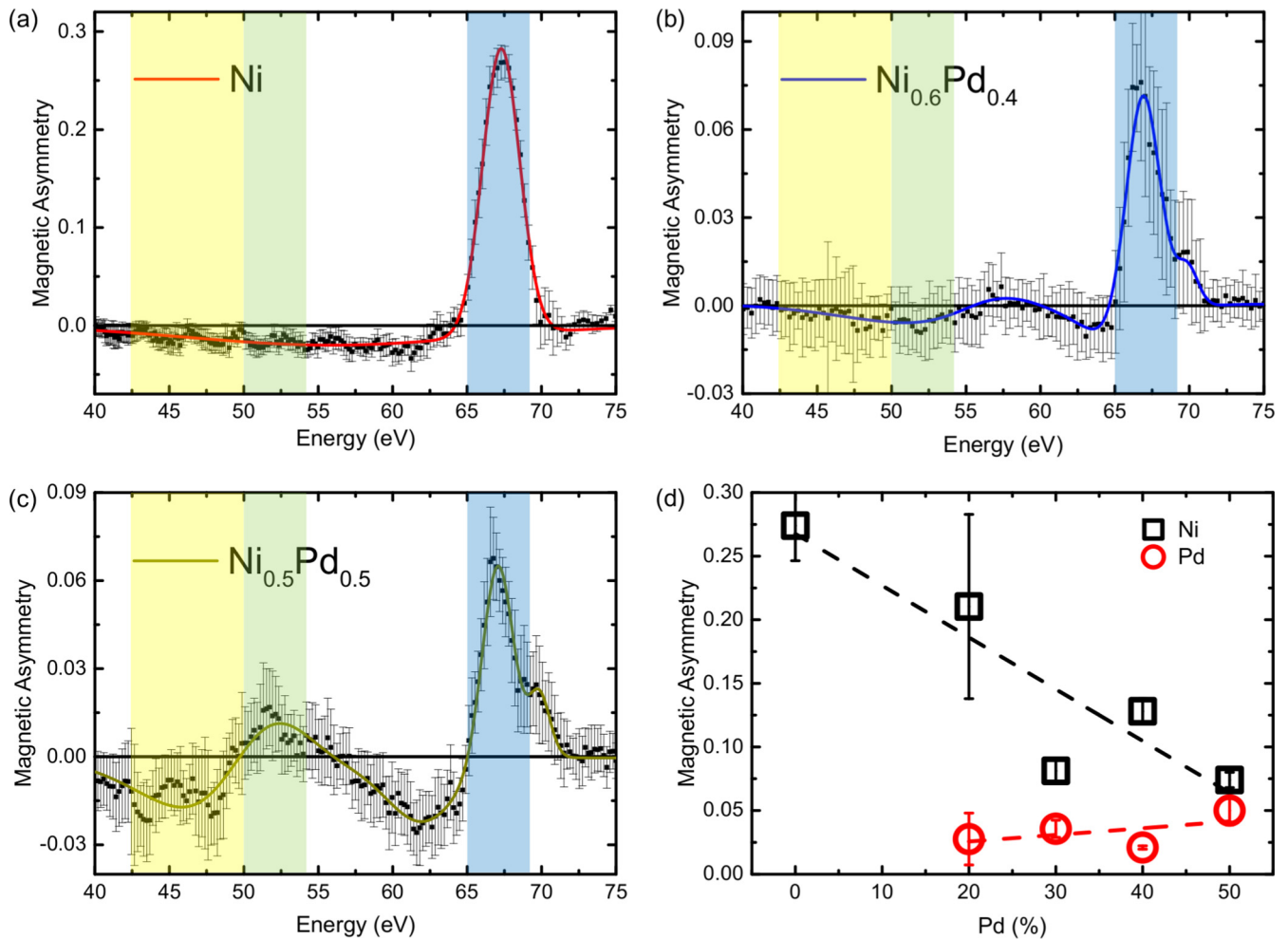


FIG. 4. Magnetic asymmetries of (a) Ni, (b) Ni<sub>0.6</sub>Pd<sub>0.4</sub>, and (c) Ni<sub>0.5</sub>Pd<sub>0.5</sub>. Ni and Pd edges are marked by blue and green/yellow rectangles, respectively. (d) Increasing Pd content results in an increase (decrease) of the Pd (Ni) asymmetry. Dashed lines are guides for the eye.

spectra, somewhat surprisingly, extends several eV beyond the tabulated resonant energy towards lower energies. We recorded consistently a clear magnetic asymmetry signature even down to 43 eV (green and yellow areas in Figs. 3 and 4). For a deeper understanding of this resonant edge broadening further insight from electronic structure theory is required. Our data analysis shows a clear positive magnetic asymmetry near the Ni absorption edge (67 eV), as well as a negative part of the magnetic asymmetry showing a broader tail extending down to  $\sim 45$  eV. In addition, the spectra show an *induced magnetic asymmetry* near the absorption edge of Pd even though Pd is an *intrinsically nonferromagnetic* material. Figure 4(a) indicates that the negative part of the bipolar signal from Ni may slightly affect the Pd magnetic asymmetry. In particular, the negative tail of the Ni signal slightly enhances the negative part of the Pd asymmetry and partly suppresses its positive part. In spite of this overlap the Pd signal is assumed to be dominant in the energy range below 55 eV in all measured Ni<sub>x</sub>Pd<sub>1-x</sub> alloys. As shown in Figs. 4(b) and 4(c), a higher Pd concentration results also in the appearance of an additional resonance peak close to the Ni absorption edge at about 70 eV.

In order to obtain a sufficient signal-to-noise ratio for the magnetic asymmetry we average over several (up to ten)

$I(H^{\downarrow,\uparrow})$  spectra before calculating the asymmetry  $A$  according to Eq. (1). After plotting the resulting magnetic asymmetry spectrum, we define  $\pm 2$  eV energy intervals around the resonance energies shown by the colored rectangles (blue for Ni and green for Pd) and a 7.5 eV energy interval below the tabulated Pd edge (yellow rectangle). We add all asymmetry data points in such an interval and divide the sum by the number of data points to calculate the average magnetic asymmetry of the given interval. The averaged asymmetry values are lower than the measured peak asymmetry in Figs. 3(b) and 4(a)–4(c). For example, Ni shows in Fig. 3(b) a magnetic asymmetry of up to 33.7%, but the average asymmetry plotted in Fig. 4(d) is only about 22%. Figure 4(d) shows the effect of increasing the Pd content on the averaged magnetic asymmetries recorded from pure Ni and a set of four Ni<sub>x</sub>Pd<sub>1-x</sub> alloys. While the positive part of the Ni asymmetry (determined in the blue energy interval) continuously drops from  $A \sim 27.4\%$  to 7.4%, the Pd signal (determined in the yellow energy interval) grows in magnitude from  $\sim 2.76\%$  to 5% upon increasing the Pd concentration from 10% to 50%.

The measured asymmetries of Ni and Ni<sub>x</sub>Pd<sub>1-x</sub> alloys shown in Fig. 4 are compared with calculated magneto-optical permittivity spectra obtained on the basis of density functional

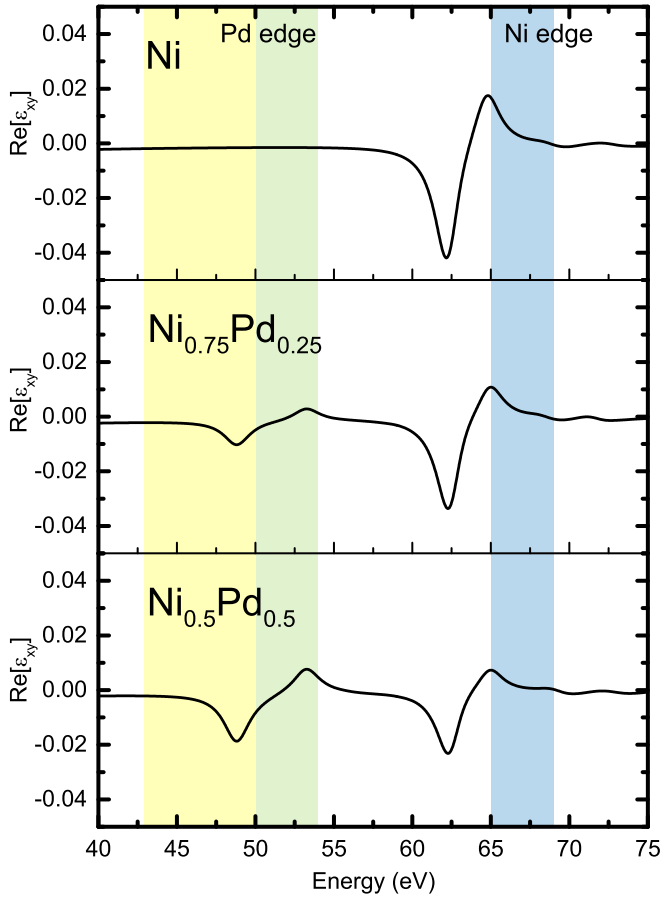


FIG. 5. Calculated absorptive part of the magneto-optical permittivity  $\text{Re}[\epsilon_{xy}(\omega)]$  of Ni (top),  $\text{Ni}_{0.75}\text{Pd}_{0.25}$  (middle), and  $\text{Ni}_{0.5}\text{Pd}_{0.5}$  (bottom) alloys based on DFT. The Ni  $M_{2,3}$  edge is located around 65 eV (near blue), and the Pd  $N_{2,3}$  edge is located around 53 eV (green and yellow). Pure Ni shows a bipolar asymmetry with a stronger amplitude in the negative part compared to the positive part. Similar to the experiment the calculated spectra show a bipolar magnetic asymmetry at the Pd  $N_{2,3}$  edge that increases in amplitude with the Pd content.

theory (DFT) in Fig. 5. The magneto-optical off-diagonal dielectric tensor element  $\epsilon_{xy}(\omega)$  and the diagonal dielectric tensor element  $\epsilon_{xx}(\omega)$  were computed using the linear response theory; the *ab initio* calculated relativistic electronic structure includes the splitting of the semicore levels due to spin-orbit and exchange interactions. The lifetime broadening of the spectra was taken to be 1 eV. For the details of the method, see Ref. [28]. The shape of the measured T-MOKE asymmetry at the Ni  $M_{2,3}$  edge shows a bipolar asymmetry with higher absolute values in the positive part than in the negative part. Comparing this shape to the computed absorptive part of the magneto-optical response, i.e., the  $\text{Re}[\epsilon_{xy}(\omega)]$  spectra shown in Fig. 5, we note that the negative part of the bipolar asymmetry is larger at the Ni  $M_{2,3}$  edge. The reason for this can be that the T-MOKE asymmetry  $A$  depends on the magneto-optical permittivity  $\epsilon_{xy}(\omega)$  as well as on the XUV index of refraction, specifically,

$$A = 2\text{Re}\left[\frac{\sin 2\theta}{n^4 \cos^2 \theta - n^2 + \sin^2 \theta} \epsilon_{xy}\right], \quad (2)$$

with  $n$  being the complex refractive index and  $\theta$  being the angle of incidence relative to the film normal [30]. Hence, the T-MOKE asymmetry can be modified by the prefactor, and in addition, there can be multiple reflections occurring in the thin films. We further note that the *ab initio* calculated magneto-optical spectrum of Ni is at a slightly lower energy (positive peak at 65 eV) than the measured T-MOKE asymmetry (peak at 67 eV). This is due to the calculated  $3p$  semicore-level energies, which can differ somewhat from measured energy positions. The computed energy position of the Pd  $4p$  states ( $N_{2,3}$  edge) compares quite well with the measured energy. The induced spin polarization on Pd leads to the appearance of the magneto-optical signal at the Pd  $N_{2,3}$  edge around 50 eV in Fig. 5. For Pd, the computed magneto-optical bipolar shape agrees well with the measured magnetic asymmetry. The  $N$ -edge magneto-optical signal increases with increasing Pd content.

### B. Element-selective spin dynamics of Ni and Pd subsystems

A unique feature of the laser-based probing employing the entire XUV spectrum is that the response of both Ni and Pd elemental subsystems can be monitored simultaneously. In particular, this parallel recording of the spin dynamics allows for testing of the presence of spin currents between the elemental subsystems, i.e., whether or not one of the subsystems can act as a spin source and the other as a spin sink [7,18,19]. Furthermore, due to the higher Pd atomic number ( $Z_{\text{Pd}} = 46$ ) compared to that of Ni ( $Z_{\text{Ni}} = 28$ ), an increased amount of Pd in the alloy is expected to result in an enhancement of spin-orbit coupling [9,31] and, consequently, in shorter demagnetization times  $\tau_M$ . To test these ideas, we first performed time-resolved measurements observing the dynamics in the Ni and Pd subsystems in the alloy films deposited on the prepatterned substrates. Figure 6 shows the result for demagnetization dynamics recorded *simultaneously* for the two elemental subsystems in the  $\text{Ni}_{0.5}\text{Pd}_{0.5}$  sample. All measured demagnetization curves were fitted with the double-exponential function

$$m(t) = 1 - \Delta m[1 - \exp(-t/\tau_M)] \exp(-t/\tau_R), \quad (3)$$

which was phenomenologically introduced to describe the time evolution of the magnetization after ultrafast optical excitation [6,32].  $\Delta m$  is the degree of magnetization quenching, and the demagnetization time  $\tau_M$  and the relaxation time  $\tau_R$  quantify how fast the sample loses and recovers magnetization after excitation by the pump pulse. Here, we focus on the demagnetization time  $\tau_M$ , for which the microscopic three-temperature model of Ref. [12] predicts a dependence on the atomic magnetic moment, the Curie temperature, and the spin-flip scattering probability.

To obtain the transient magnetization dynamics in the Pd subsystem, the negative part (yellow) of the Pd asymmetry has been taken. All measured stoichiometries ( $x = 1.0, \dots, 0.5$ ) show qualitatively the same spectral behavior with the Pd (Ni) signal continuously increasing (decreasing) with increasing Pd concentration [see Fig. 4(d)]. For Pd concentrations above 50% the T-MOKE signal drops again, now due to the fact that the magnetization of the alloy films rotates out of plane [33]. Variations of the magnetic asymmetries of the samples with Pd

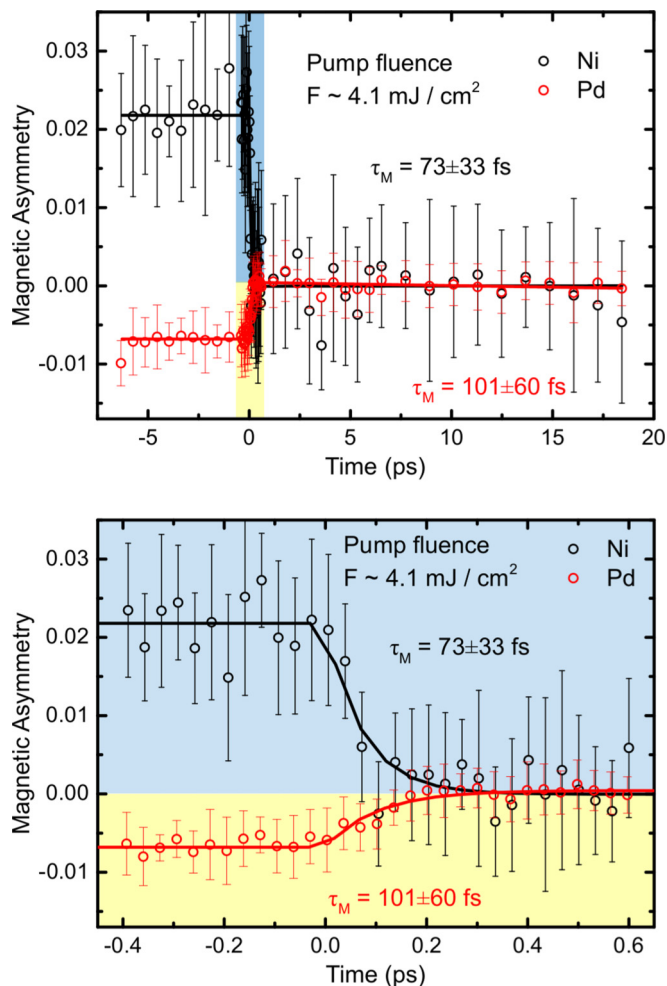


FIG. 6. Spin dynamics measured at the Ni and Pd absorption edges in the  $\text{Ni}_{0.5}\text{Pd}_{0.5}$  alloy. Black and red symbols represent experimental values for Ni and Pd, respectively, which are simultaneously obtained from the measured XUV spectra. Solid lines are the double-exponential fits from which  $\tau_M$  values were extracted. The lower figure is a magnification of the colored time interval around  $t = 0$  marked in the upper graph. The  $\text{Ni}_{0.5}\text{Pd}_{0.5}$  alloy was pumped with the laser fluence  $F \sim 4.1 \text{ mJ/cm}^2$ . Both Ni and Pd subsystems show a complete demagnetization, with Ni demagnetizing faster than Pd. Slow recovery times  $\tau_R$  in the range of hundreds of picoseconds to several nanoseconds have been observed for both subsystems in a separate measurement (not included).

content less than 50%, triggered by the optical excitation, are therefore in the first approximation assumed to represent the dynamics of the Pd elemental subsystem. Our time-resolved data show that both the Ni and Pd subsystems demagnetize, with Ni showing an about 30% faster demagnetization time compared to Pd. This fact may lead to the conclusion that the Pd subsystem is slower and “follows” the spin dynamics of Ni. However, for Pd concentrations below 50%, the Pd signal is weak, which leads to an appreciable scattering of the  $\tau_M$  values, making it difficult to confirm the slower Pd response and possible stoichiometry dependence. On the other hand, all measured transients consistently show demagnetization of both Ni and Pd subsystems in the entire concentration range, which may again lead to the conclusion that, for

the chosen laser fluence, there is no clearly detectable spin rearrangement between the Ni and Pd subsystems induced by spin current.

Previously, spin currents arising from ultrafast laser-induced demagnetization have been observed between laterally separated sample areas [15], between adjacent metallic layers [7,34], and between different sublattices in ferrimagnetic rare-earth-transition-metal films [18,35]. In the latter observation, it was shown that the total angular momentum of the two sublattices stays constant in the initial phase after the laser excitation due to transfer of angular momentum from the transition-metal atoms, where the spin-polarized  $3d$  states are strongly excited by the laser, to the lanthanide atoms, where the deep-lying  $4f$  states are not immediately excited by the laser. After the initial conservation of angular momentum, thermally dominated demagnetization sets in. For our  $\text{Ni}_x\text{Pd}_{1-x}$  alloys, however, we cannot confirm a similar effect. In the presence of *ferromagnetic* coupling expected from the less than 10% decrease of the magnetic moment up to 45% of Pd content in the alloy [24], similar to what is described in Ref. [7], a spin current would result in an *enhancement* of the magnetic signal at one of the absorption edges. Even by lowering the laser fluence up to a complete disappearance of the Pd signal (results not shown), we did not observe this effect. We conclude that an optically triggered spin current between the subsystems is not dominating the spin dynamics in our sample system. Rather, the demagnetization of Pd follows the Ni demagnetization, possibly with a slower demagnetization rate. This suggests that a local demagnetization mechanism on both Ni and Pd plays an important role.

In the next section we investigate the influence of the increased spin-orbit coupling (SOC) on the dynamics. Because the signal from Pd is weak at low concentrations of Pd (0% to 40%), our study focuses on the dynamics of the Ni subsystem by tracing the spectral changes near 67 eV (Ni edge) induced by the optical pumping.

### C. Spin dynamics in the Ni subsystem

As introduced above, the demagnetization time has been proposed [12] to scale with atomic magnetic moment  $\mu_{\text{AT}}$ , spin-flip probability  $a_{\text{sf}}$ , and Curie temperature  $T_C$  as  $\tau_M \sim \mu_{\text{AT}}/a_{\text{sf}}T_C$  if we assume that the phonon bath temperature  $T_p$  is constant in the considered time interval. While, with an increasing amount of Pd in the  $\text{Ni}_x\text{Pd}_{1-x}$  alloy, the slowly varying  $\mu_{\text{AT}}$  is expected to have a negligible effect on  $\tau_M$ , the sizable decrease in  $T_C$  is expected to lead to a  $\tau_M$  increase if we assume a constant  $a_{\text{sf}}$ . However, because  $a_{\text{sf}}$  scales with the nuclear charge  $Z$  as  $a_{\text{sf}} \propto Z^4$  and  $Z_{\text{Pd}} = 46$  is almost twice as large as  $Z_{\text{Ni}} = 28$ ,  $\tau_M$  is expected to be strongly affected by  $a_{\text{sf}}$  as well, depending thus on the  $\text{Ni}_x\text{Pd}_{1-x}$  stoichiometry [12,31]. In particular, for increasing Pd content the increasing  $a_{\text{sf}}$  can (over)compensate the effect of the decreasing  $T_C$  on  $\tau_M$  and thus drive the  $\text{Ni}_x\text{Pd}_{1-x}$  dynamics into a completely opposite dependence on composition resulting in a  $\tau_M$  decrease with increasing Pd content. We note that the  $a_{\text{sf}}$  variation is predominantly governed by the increasing amount of Pd. Therefore, measuring the  $\tau_M$  variation in the Pd subsystem might be a more direct signature of this tendency. However, at low Pd concentrations, the T-MOKE signal at the Pd absorption

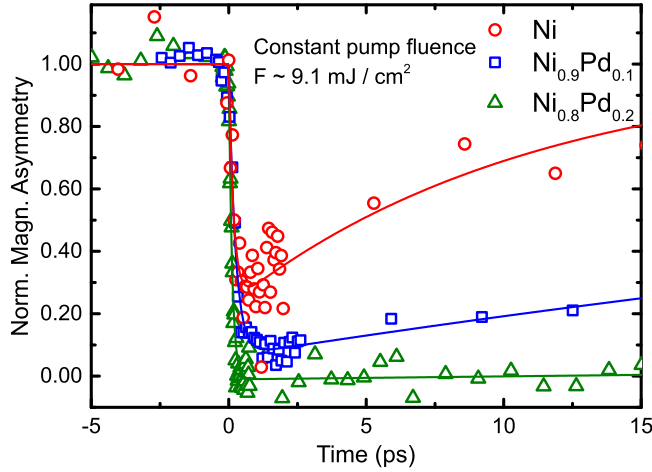


FIG. 7. Spin dynamics of the Ni subsystem measured for two different  $\text{Ni}_x\text{Pd}_{1-x}$  alloy compositions and compared to the pure Ni response. The data are measured with T-MOKE at the Ni  $M_{2,3}$  absorption edge with a constant pump fluence of  $F \sim 9.1 \text{ mJ/cm}^2$ . Solid lines are fits to Eq. (3), which yield relaxation times  $\tau_R$  between 11 ps for pure Ni and about 1 ns for  $\text{Ni}_{0.8}\text{Pd}_{0.2}$ .

edge is weak, leading to a signal-to-noise ratio too small to determine  $\tau_M$  values with the required precision. The fact that the magnetic moment of Pd is induced due to the proximity of Ni implies a strong coupling between the Pd and Ni subsystems. Hence, an  $a_{sf}$  variation is expected to affect the Ni response, too. Therefore, we focus exclusively on the dynamics of the Ni elemental subsystem in the following. Note that the Ni-Pd exchange coupling is assumed to be constant at this time, although it may vary with stoichiometry as well. In the first step, we investigated the response of the Ni subsystem to constant pump fluence in samples with different compositions. Figure 7 shows corresponding demagnetization curves for Pd contents of 0%, 10%, and 20%. Magnetic asymmetries were first calculated using Eq. (1). The curves were then normalized by setting the initial asymmetries (before zero time delay) of all the samples to unity in order to trace the dynamics as a function of alloy composition (the same procedure was used to produce Fig. 8). With increasing Pd content, the optically induced transients show both a higher quenching and a slower relaxation of the magnetization. This observation can be interpreted as a consequence of the change in the relative temperature  $T/T_C$ , as was shown by Roth *et al.* [36]. In our case, the Curie temperature  $T_C$  is tuned instead of the sample temperature  $T$  as in Ref. [36]. Nevertheless, the relaxation time and quenching appear to scale with the  $T/T_C$  ratio in a manner similar to that reported in Ref. [36].

In order to exclude that a stoichiometry-dependent absorption of the pump probe gives rise to the observed changes, the reflectance of pure Ni as well as  $\text{Ni}_x\text{Pd}_{1-x}$  alloys ( $x = 0.5, 0.6, 0.7, 0.9$ ) was measured at a wavelength of 800 nm (1.55 eV). Due to the very thick substrate we can safely assume that there is no transmission, and therefore, the light is mostly absorbed and reflected by the samples. Reflectance measurements were performed at room temperature and in ambient atmosphere (not in vacuum). The power of the incoming light is 8.76 mW, and the angle of incidence is  $45^\circ$ . The reflectance

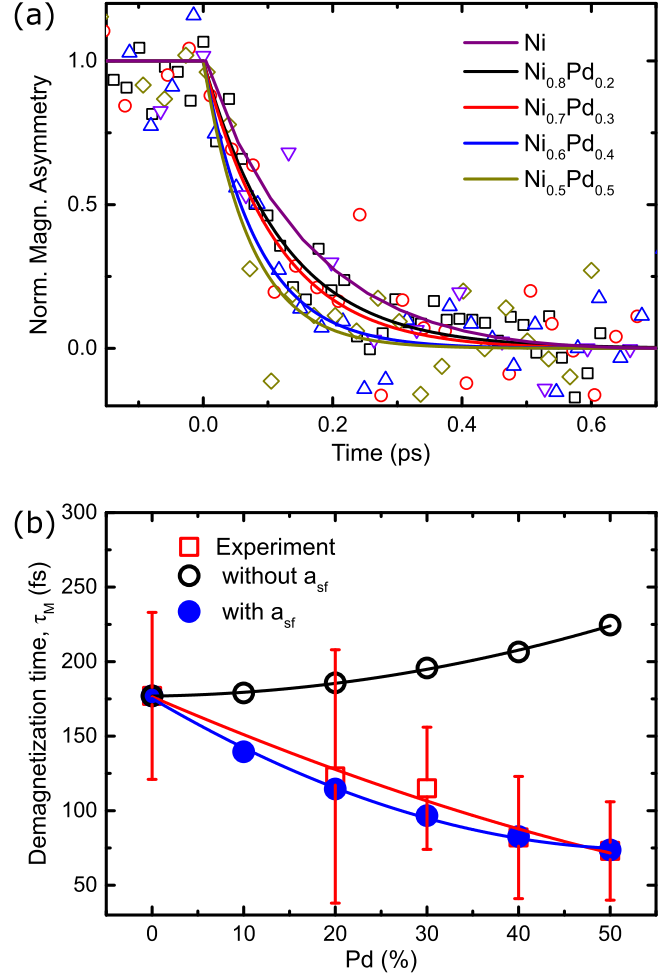


FIG. 8. (a) Normalized demagnetization curves measured at the Ni  $M_{2,3}$  edge in alloys with varying composition. Laser pump fluence for all measurements (excluding pure Ni) was adjusted to trigger full quenching. (b) Comparison of the experimentally determined  $\tau_M$  variations (red) with the scaling according to the M3TM without SOC ( $\mu_{AT}/T_C$  scaling, black) and with SOC ( $\mu_{AT}/a_{sf}T_C$  scaling, blue). Solid lines are guides for the eye.

of the measured alloys ranges from 71.35% to 73.06% and seems to decrease slightly with increasing Pd content. Thus, the stoichiometry-dependent variation of reflectance is less than 2%, which is relatively small compared to the 30% decrease of the Curie temperature from Ni to  $\text{Ni}_{0.5}\text{Pd}_{0.5}$  [24]. Therefore, we conclude that the demagnetization of Ni and  $\text{Ni}_x\text{Pd}_{1-x}$  alloys is not affected by stoichiometry-dependent light absorption.

In order to investigate the ultrafast demagnetization regime, we performed a series of measurements in which we increased the laser pump fluence for each alloy composition individually until *full quenching* was reached in order to minimize the effect of the quenching amplitude on the demagnetization time constant [12]. In the case of the pure Ni film, however, due to its higher  $T_C$ , we reached only 70% quenching with the maximum available pump intensity. Figure 8(a) shows transient measurements performed at the Ni absorption edge for different compositions. Open symbols show the experiment, and solid

TABLE I. Stoichiometry-dependent demagnetization times  $\tau_M$  measured at the Ni absorption edge.

Stoichiometry	Demagnetization time $\tau_M$
Ni	$177 \pm 56$ fs
Ni <sub>0.8</sub> Pd <sub>0.2</sub>	$123 \pm 85$ fs
Ni <sub>0.7</sub> Pd <sub>0.3</sub>	$115 \pm 41$ fs
Ni <sub>0.6</sub> Pd <sub>0.4</sub>	$82 \pm 41$ fs
Ni <sub>0.5</sub> Pd <sub>0.5</sub>	$73 \pm 33$ fs

curves represent double-exponential fits to the function given in Eq. (3), from which  $\tau_M$  values have been extracted. In order to compare the responses for different compositions we normalized the demagnetization curves to equal 1 for the signal before excitation and 0 for the complete demagnetization. We note that the demagnetization time for the fully quenched pure Ni system is expected to be slightly longer than the one presented for 70% quenching, nevertheless complying with the observed dependence of  $\tau_M$  on varying Ni<sub>x</sub>Pd<sub>1-x</sub> composition [12,31]. The measured stoichiometry-dependent  $\tau_M$  values are plotted in Fig. 8(b) as red squares and are compiled in Table I.

This measurement is an experimental confirmation of the fact that SOC has to be taken into account when discussing  $\tau_M$  variations on femtosecond time scales. We stress again that exclusively considering variations of  $T_C$  with alloy stoichiometry, without SOC, would lead to a completely opposite  $\tau_M$  dependence. This is indicated in Fig. 8(b), where the red open squares represent our experiment, black open circles show a qualitative prediction made on the basis of the M3TM without SOC (only  $\mu_{AT}/T_C$  scaling), and blue circles indicate the  $\tau_M$  variation with stoichiometry taking SOC into account ( $\mu_{AT}/a_{sf}T_C$  scaling including  $a_{sf}$  variation).

Below we briefly discuss the procedure for obtaining the curves describing the theoretical models shown in Fig. 8(b). To obtain the predicted tendencies, we first estimated values for  $\mu_{AT}$  and  $T_C$  from Ref. [24]. Thus, compared to pure Ni, adding 50% of Pd results in a drop in the magnetic moment  $\mu_{AT}$  by about 10% and a decrease in the Curie temperature  $T_C$  by approximately 29%. Furthermore, as noted above, the relative change in the spin-flip probability is assumed to scale with  $a_{sf} \propto Z^4$  according to SOC [9]. To get the effective  $Z$  we linearly interpolated between  $Z_{Ni} = 28$  and  $Z_{Pd} = 46$  according to the alloy composition:  $Z_{Ni_xPd_{1-x}} = xZ_{Ni} + (1-x)Z_{Pd}$  [9]. For equiatomic Ni<sub>0.5</sub>Pd<sub>0.5</sub>, we therefore obtain  $Z_{Ni_0.5Pd_0.5}^4 = [(Z_{Ni} + Z_{Pd})/2]^4 = 37^4$ , resulting in an estimated increase in effective  $a_{sf}$  of over 200% compared to pure Ni ( $Z_{Ni}^4 = 28^4$ ). In order to apply the scaling law to the experimental  $\tau_M$  values, we rewrite the scaling  $\tau_M \sim \mu_{AT}/(a_{sf}T_C)$  as  $\tau_M \sim \mu_{AT}/(Z^4T_C)$ . Then we calculate for each composition  $x$  in Fig. 8(b)  $A_1\mu_{AT}/(Z^4T_C)$  (including SOC, solid blue circles) and  $A_2\mu_{AT}/T_C$  (without SOC, open black circles), employing  $\mu_{AT}$  and  $T_C$  values from Ref. [24] and the effective  $Z_{Ni_xPd_{1-x}}$  introduced above. The proportionality factors  $A_1$  and  $A_2$  are determined from our experimental data point for pure Ni.

Our findings in Fig. 8(b) accentuate the fact that  $a_{sf}$  due to Pd-mediated SOC may play a critical role in the determination of demagnetization time based on the M3TM. We note in this

respect that *ab initio* calculations of the electron-phonon spin-flip scattering did confirm the existence of the electron-phonon spin-flip scattering mechanism assumed in the M3TM, but the thus-computed demagnetization rates were smaller than the measured demagnetization rates, indicating the presence of other spin dissipation channels [37]. The *ab initio* calculations did, however, show that photon-driven creation of deep-lying holes in combination with SOC causes a faster demagnetization [37]. This strong dependence of the spin-flip scattering of deep-lying holes on the SOC is consistent with our observations.

## V. CONCLUSION

In conclusion, our measurements demonstrate that the spectrum of extreme ultraviolet light generated by a femtosecond laser amplifier can be employed to explore in substantial detail the spin dynamics in complex ferromagnetic materials in a laboratory-based experiment. In particular, we first demonstrate the element-selective measurement of magnetic T-MOKE asymmetry in a magnetic alloy, in which one sublattice is formed by an elemental paramagnet. Static measurements of magnetic asymmetry show that the Pd sublattice in Ni<sub>x</sub>Pd<sub>1-x</sub> becomes *ferromagnetic* with magnetic asymmetries up to 4.6% that extend substantially beyond the tabulated energy values for the Pd absorption edge. The signal cross talk in the energy interval between the Ni and Pd absorption edges is small compared to the asymmetry at the absorption edges and does not inhibit obtaining separate element-selective signals from the two elemental subsystems. Optical excitation of all investigated alloy compositions using 1.55 eV photons shows that both Ni and Pd subsystems experience optically induced demagnetization. Although in our experiments we saw no direct signature of a spin transfer between the sublattices, its presence cannot be dismissed entirely, and it may be present in the systems with higher Pd concentration (>50%) or at different pump laser fluence. The dynamics of the Ni subsystem shows a strong *demagnetization time decrease* from  $\tau_M \sim 177$  fs to  $\tau_M \sim 73$  fs upon increasing the Pd content in the alloy from 0% to 50%, indicating a strong coupling between the Ni and Pd magnetic sublattices and an important impact of spin-orbit coupling on the ultrafast demagnetization. On the other hand, the indication of different Ni and Pd demagnetization times in Ni<sub>x</sub>Pd<sub>1-x</sub> alloys suggests a partial decoupling of the induced Pd moment from the Ni moment at femtosecond time scales. Based on our experimental observations, we suggest that the strong decrease of the demagnetization time with Pd content can be explained by considering the decisive role of the spin-flip scattering probability  $a_{sf}$ , which due to spin-orbit coupling is strongly dependent on the alloy composition.

## ACKNOWLEDGMENTS

The authors gratefully acknowledge financial support from the DFG project SCHN 353/17-1: “Element-spezifische Untersuchung von Femtosekunden Magnetisierungsdynamik” and from the Swedish Research Council (VR), the K. and A. Wallenberg Foundation (Grant No. 2015.0060), and the Swedish National Infrastructure for Computing (SNIC).



- [1] E. Beaurepaire, J.-C. Merle, A. Daunois, and J.-Y. Bigot, *Phys. Rev. Lett.* **76**, 4250 (1996).
- [2] J. Hohlfeld, E. Matthias, R. Knorren, and K. H. Bennemann, *Phys. Rev. Lett.* **78**, 4861 (1997).
- [3] J. Güdde, U. Conrad, V. Jähnke, J. Hohlfeld, and E. Matthias, *Phys. Rev. B* **59**, R6608 (1999).
- [4] B. Koopmans, M. van Kampen, J. T. Kohlhepp, and W. J. M. de Jonge, *Phys. Rev. Lett.* **85**, 844 (2000).
- [5] C. La-O-Vorakiat, M. Siemens, M. M. Murnane, H. C. Kapteyn, S. Mathias, M. Aeschlimann, P. Grychtol, R. Adam, C. M. Schneider, J. M. Shaw, H. Nembach, and T. J. Silva, *Phys. Rev. Lett.* **103**, 257402 (2009).
- [6] S. Mathias, L.-O. Chan, P. Grychtol, P. Granitzka, E. Turgut, J. M. Shaw, R. Adam, H. T. Nembach, M. E. Siemens, S. Eich *et al.*, *Proc. Natl. Acad. Sci. USA* **109**, 4792 (2012).
- [7] D. Rudolf, L.-O. Chan, M. Battiato, R. Adam, J. M. Shaw, E. Turgut, P. Maldonado, S. Mathias, P. Grychtol, H. T. Nembach *et al.*, *Nat. Commun.* **3**, 1037 (2012).
- [8] E. Turgut, J. M. Shaw, P. Grychtol, H. T. Nembach, D. Rudolf, R. Adam, M. Aeschlimann, C. M. Schneider, T. J. Silva, M. M. Murnane *et al.*, *Phys. Rev. Lett.* **110**, 197201 (2013).
- [9] F. Willems, C. T. L. Smeenk, N. Zhavoronkov, O. Kornilov, I. Radu, M. Schmidbauer, M. Hanke, C. von Korff Schmising, M. J. J. Vrakking, and S. Eisebitt, *Phys. Rev. B* **92**, 220405(R) (2015).
- [10] B. Pfau, S. Schaffert, L. Müller, C. Gutt, A. Al-Shemmary, F. Büttner, R. Delaunay, S. Düsterer, S. Flewett, R. Frömter *et al.*, *Nat. Commun.* **3**, 1100 (2012).
- [11] C. von Korff Schmising, B. Pfau, M. Schneider, C. M. Günther, M. Giovannella, J. Perron, B. Vodungbo, L. Müller, F. Capotondi, E. Pedersoli, N. Mahne, J. Lüning, and S. Eisebitt, *Phys. Rev. Lett.* **112**, 217203 (2014).
- [12] B. Koopmans, G. Malinowski, F. D. Longa, D. Steiauf, M. Fähnle, T. Roth, M. Cinchetti, and M. Aeschlimann, *Nat. Mater.* **9**, 259 (2010).
- [13] M. Battiato, K. Carva, and P. M. Oppeneer, *Phys. Rev. Lett.* **105**, 027203 (2010).
- [14] T. Kampfrath, M. Battiato, P. Maldonado, G. Eilers, J. Nötzold, S. Mährlein, V. Zbarsky, F. Freimuth, Y. Mokrousov, S. Blügel *et al.*, *Nat. Nanotechnol.* **8**, 256 (2013).
- [15] I. Radu, K. Vahaplar, C. Stamm, T. Kachel, N. Pontius, H. A. Dürr, T. A. Ostler, J. Barker, R. F. L. Evans, R. W. Chantrell *et al.*, *Nature (London)* **472**, 205 (2011).
- [16] J. H. Mentink, J. Hellsvik, D. V. Afanasiev, B. A. Ivanov, A. Kirilyuk, A. V. Kimel, O. Eriksson, M. I. Katsnelson, and T. Rasing, *Phys. Rev. Lett.* **108**, 057202 (2012).
- [17] V. G. Bar'yakhtar, *Zh. Éksp. Teor. Fiz.* **87**, 1501 (1984) [*Sov. Phys. JETP* **60**, 863 (1984)].
- [18] N. Berggaard, V. López-Flores, V. Halté, M. Hehn, C. Stamm, N. Pontius, E. Beaurepaire, and C. Boeglin, *Nat. Commun.* **5**, 4466 (2014).
- [19] C. E. Graves, A. H. Reid, T. Wang, B. Wu, S. De Jong, K. Vahaplar, I. Radu, D. P. Bernstein, M. Messerschmidt, L. Müller *et al.*, *Nat. Mater.* **12**, 293 (2013).
- [20] V. G. Bar'yakhtar, V. I. Butrim, and B. A. Ivanov, *JETP Lett.* **98**, 289 (2013).
- [21] J. Y. Chauleau, B. J. McMorran, R. Belkhou, N. Berggaard, T. O. Menteş, M. A. Nino, A. Locatelli, J. Unguris, S. Rohart, J. Miltat *et al.*, *Phys. Rev. B* **84**, 094416 (2011).
- [22] D. L. Windt, *Comput. Phys.* **12**, 360 (1998).
- [23] [http://henke.lbl.gov/optical\\_constants/filter2.html](http://henke.lbl.gov/optical_constants/filter2.html).
- [24] H. P. J. Wijn, *Magnetic Properties of Metals: D-Elements, Alloys and Compounds* (Springer, Berlin, 1991).
- [25] H. Ibach and H. Lüth, *Festkörperphysik. Einführung in die Grundlagen* (Springer-Verlag, Berlin, Heidelberg, 2009).
- [26] H. C. Kapteyn, M. M. Murnane, and I. P. Christov, *Phys. Today* **58**(3), 39 (2005).
- [27] P. Grychtol, R. Adam, S. Valencia, S. Cramm, D. E. Bürgler, and C. M. Schneider, *Phys. Rev. B* **82**, 054433 (2010).
- [28] M. Hecker, P. M. Oppeneer, S. Valencia, H. C. Mertins, and C. M. Schneider, *J. Electron Spectrosc. Relat. Phenom.* **144**, 881 (2005).
- [29] S. Valencia, A. Kleibert, A. Gaupp, J. Rusz, D. Legut, J. Bansmann, W. Gudat, and P. M. Oppeneer, *Phys. Rev. Lett.* **104**, 187401 (2010).
- [30] P. M. Oppeneer, in *Handbook of Magnetic Materials* (Elsevier, Amsterdam, 2001), pp. 229–422.
- [31] K. C. Kuiper, T. Roth, A. J. Schellekens, O. Schmitt, B. Koopmans, M. Cinchetti, and M. Aeschlimann, *Appl. Phys. Lett.* **105**, 202402 (2014).
- [32] I. Radu, G. Woltersdorf, M. Kiessling, A. Melnikov, U. Bovensiepen, J.-U. Thiele, and C. H. Back, *Phys. Rev. Lett.* **102**, 117201 (2009).
- [33] M. Plötzing, Master's thesis, Rheinisch-Westfälische Technische Hochschule Aachen, 2011.
- [34] A. Melnikov, I. Razdolski, T. O. Wehling, E. T. Papaioannou, V. Roddatis, P. Fumagalli, O. Aktsipetrov, A. I. Lichtenstein, and U. Bovensiepen, *Phys. Rev. Lett.* **107**, 076601 (2011).
- [35] S. Wienholdt, D. Hinzke, K. Carva, P. M. Oppeneer, and U. Nowak, *Phys. Rev. B* **88**, 020406 (2013).
- [36] T. Roth, A. J. Schellekens, S. Alebrand, O. Schmitt, D. Steil, B. Koopmans, M. Cinchetti, and M. Aeschlimann, *Phys. Rev. X* **2**, 021006 (2012).
- [37] K. Carva, M. Battiato, and P. M. Oppeneer, *Phys. Rev. Lett.* **107**, 207201 (2011).